MONAZITE-FLUORAPATITE CHARACTERISTICS AS EVIDENCE FOR INTERPLAY BETWEEN ~2.04 GA FLUID-INDUCED DEHYDRATION AND MELTING OF THE SAND RIVER GNEISS, LIMPOPO COMPLEX, SOUTH AFRICA

H.M. RAJESH
Department of Earth and Environmental Sciences, BIUST, Botswana
e-mail: rajesh.hm@biust.ac.bw

O.G. SAFONOV
Institute of Experimental Mineralogy RAS, Chernogolovka, Russia
Department of Geology, University of Johannesburg, P.O. Box 524, Auckland Park, 2001, South Africa
e-mail: oleg@iem.ac.ru

G.A. BELYANIN AND J.D. KRAMERS
Department of Geology, University of Johannesburg, P.O. Box 524, Auckland Park, 2001, South Africa
e-mail: gbelyanin@gmail.com; jkramers@uj.ac.za

ABSTRACT

A tonalitic vein from a representative traverse section from the Paleoarchean Sand River biotite-amphibole gneiss consists of two domains – orthopyroxene-bearing and orthopyroxene-absent domains – which grade from center to the margin, along its length. The orthopyroxene-bearing domain is heavily altered with respect to the surrounding orthopyroxene-absent domain, which preserves a prominent magmatic texture typical of crystallized melt. Contrasting textures were observed in terms of monazite occurrence in fluorapatite in the two domains. While monazite occurs as inclusions in fluorapatite in the orthopyroxene-bearing domain, it prominently occurs as irregular rims along fluorapatite margins in the orthopyroxene-absent domain. The textural relation of monazite, occurring as both inclusions and irregular rims in the same fluorapatite grains, and different mineral chemical characteristics of both types of monazite, supports the operation of melting accompanying fluid-induced dehydration in the Sand River orthogneiss. T-aH$_2$O pseudosection modeling reproduced the mineral assemblages of the domain representing melt portion formed during dehydration. The Paleoproterozoic timing of the events is characterized by a ^{40}Ar/^{39}Ar amphibole age of 2037 ± 10 Ma from the dehydrated gneiss.

Introduction

In comparison to garnet, orthopyroxene and clinopyroxene are relatively rare within leucosomes in migmatitic gneisses. The pyroxene-bearing assemblages are commonly surrounded by felsic melt in a patchy irregular distribution (e.g., Clarke et al., 2007) or along the center of felsic melt-bearing veins (e.g., Rajesh et al., 2013). In either case, the volume proportion of melt is small. Usually the formation of orthopyroxene in small-volume, melt-bearing migmatitic gneisses is considered as products of fluid-absent dehydration melting (e.g., Waters, 1988; Clarke et al., 2007). Fluid induced melting involving H$_2$O-rich fluids is less likely in such cases, as it will produce voluminous melt (e.g., Prince et al., 2001). But if the felsic-melt bearing veins occupy former ductile shear zones, it is not implausible to consider a fluid-present alternative, in which the orthopyroxene is a product of dehydration by a relatively low-aH$_2$O fluid (e.g., Pattison, 1991; Hansen and Stuk, 1993; Perchuk et al., 2000; Rajesh et al., 2013). In this case, the formation of pyroxene-bearing assemblages via metasomatism either preceded or was accompanied by partial melting, resulting in small-volumes of felsic melts with pyroxene-bearing dehydration zones.

A scenario in which partial melting seems to be a natural progression of the preceding fluid-induced dehydration of biotite-amphibole gneiss was recently described by Safonov et al. (2012) and Rajesh et al. (2013) from the Limpopo Complex in South Africa. The present study follows these two studies and presents new detailed textural and mineral chemical data on monazite-fluorapatite relations supportive of melting accompanying fluid induced dehydration of the orthogneiss, results of thermodynamic modelling of the assemblages in the solidus and sub-solidus stages of these processes, and an ^{40}Ar/^{39}Ar amphibole age to constrain the timing of events. Considering that element transport by either low-aH$_2$O fluid or melt from grain boundaries to centimetric- and metric-scale veins

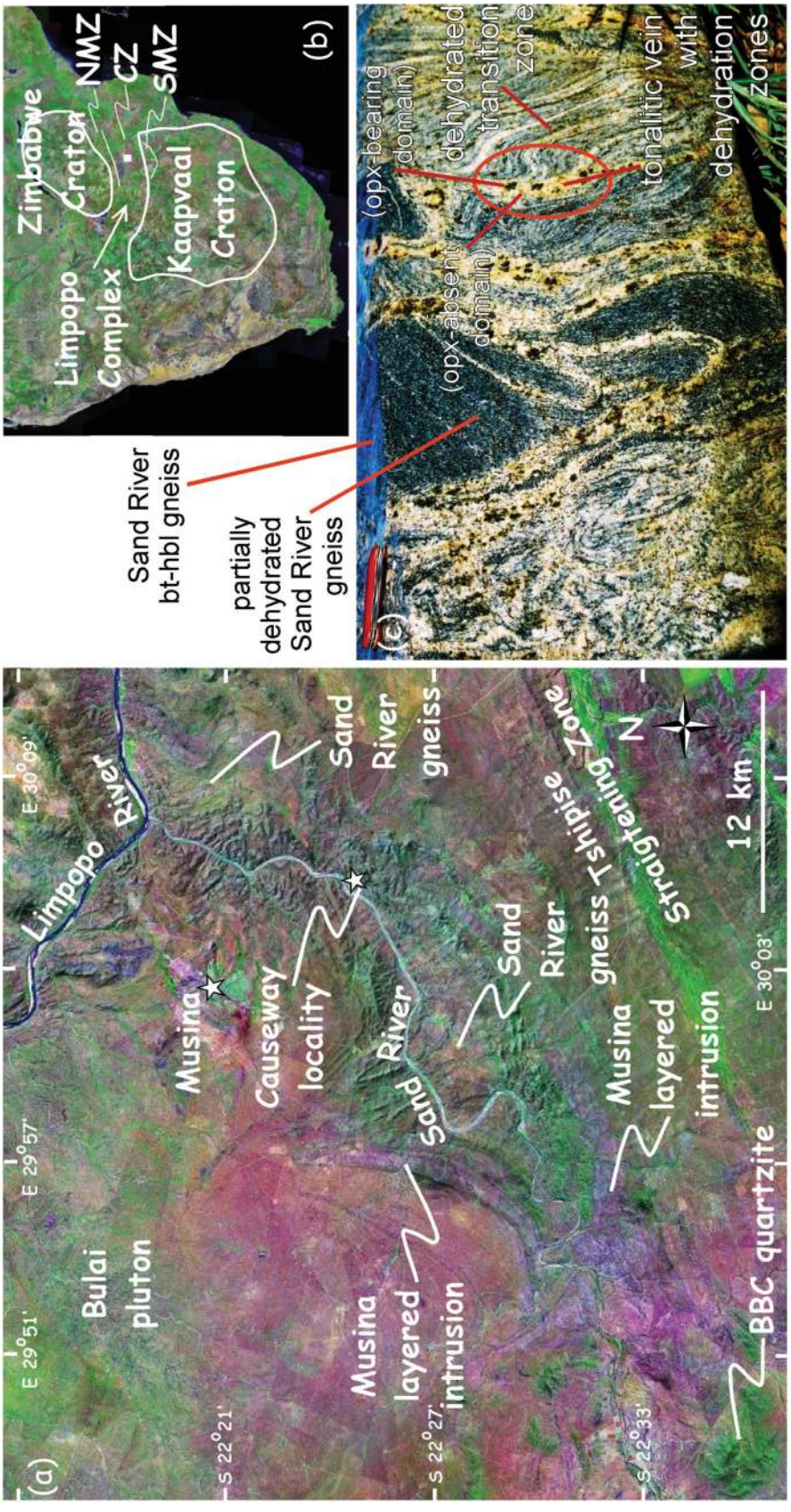
(a)
E 29°51'
E 29°57'
E 30°09'
E 30°03'
S 22°21'
S 22°27'
S 22°33'
Limpopo River
Bulai pluton
Musina
Causeway locality
Sand River
Sand River gneiss
Musina layered intrusion
Sand River gneiss Tshipise Zone
Straightening
Musina layered intrusion
BBC quartzite
N
12 km
(b)
Zimbabwe Craton
NMZ
CZ
SMZ
Limpopo Complex
Kaapvaal Craton
Sand River bt-hbl gneiss
partially dehydrated Sand River gneiss
(c)
(opx-bearing domain)
(opx-absent domain)
dehydrated transition zone
tonalitic vein with dehydration zones

involves understanding of the detailed textural and chemical characterization of minerals, especially accessory minerals, our results on the chemistry of REE-partitioning minerals such as fluorapatite and monazite is significant.

Geologic setting

Central Zone of the Limpopo Complex

The Sand River gneiss traverse section studied here is exposed at the Causeway locality, southeast of Musina, within the Central Zone of the Limpopo Complex in South Africa (Figure 1). The Central Zone, occupying the largest area of the three sub zones of the Limpopo Complex, comprises a variety of deformed supracrustal rocks (Beit Bridge Complex) and minor mafic to ultramafic rocks (Musina layered intrusion), which are tectonically interleaved within voluminous granitoid orthogneisses, including the Sand River tonalite-trondhjemite-granodiorite gneiss (Figures 1a and b; see review in Smit et al., 2011). Available geochronological data indicate that the Central Zone was affected by at least three high-grade tectono-metamorphic events, at ~3.24 to 3.15 Ga, ~2.66 to 2.61 Ga and ~2.04 to 2.01 Ga (see reviews in Smit et al., 2011; Kramers et al., 2011).

Sand River gneiss at the Causeway locality

The Sand River gneiss exposed at the Causeway locality is generally well-banded, migmatitic and interlayered with the Beit Bridge Complex paragneisses (Fripp, 1983). The intrusive relation of the Sand River gneiss with the Beit Bridge Complex supracrustal rocks and rocks of the Musina layered intrusion is evident from the presence of inclusions of the latter in the former. Based on U-Pb zircon ages obtained from the Causeway locality, Retief et al. (1990); Tsunogae and Yurimoto (1995); Jaeckel et al. (1997); Kröner et al. (1998, 1999); Zeh et al. (2007); Gerdes and Zeh (2009) and Zeh et al. (2010) constrained the magmatic crystallization age of the Sand River gneiss at ~3.31 to 3.27 Ga. Different studies showed that the Sand River orthogneiss preserves evidence (zircon overgrowths) for at least two periods of metamorphic zircon growth – one at ~2.66 to 2.61 Ga and another at ~2.03 to 2.01 Ga (Retief et al., 1990; Jaeckel et al., 1997; Kröner et al., 1999; Zeh et al., 2007, 2010; Gerdes and Zeh, 2009). A third high-grade event at ~3.14 Ga is probable (Zeh et al., 2007; Gerdes and Zeh, 2009). The Neoarchean tectono-metamorphic event in the Sand River orthogneiss correlates well with meter-sized bodies of Neoarchean (~2.68 to 2.57 Ga; Jaeckel et al., 1997; Kröner et al., 1999; Zeh et al., 2007; Van Reenen et al., 2008) garnet-bearing Singelele-type gneiss, considered as products of local anatexis, and occurring interlayered and interfolded with earlier rocks at the Causeway locality. The Paleoproterozoic tectono-metamorphic event is correlated with undeformed leucosome patches and veins (Jaeckel et al., 1997), and irregular bodies of biotite-bearing granite pegmatites (Jaeckel et al., 1997; Zeh et al., 2010).

The present study focuses on the Paleoproterozoic leucosome patches and veins, which are minor in volume relative to the older melt-bearing bodies. These more or less *in situ* leucosome patches and veins developed along small-scale ductile shear zones that are oblique to the fabric in the host Sand River gneiss, and are characterized by distinct orthopyroxene-bearing domains.

Fluid-induced dehydration of the Sand River gneiss

A representative traverse section containing the orthopyroxene-bearing tonalitic leucosome veins (Figure 1c) consists of macroscopically distinct rock types that preserve evidence for progressive stages of fluid-induced dehydration of the pyroxene-absent Sand River gneiss to the pyroxene-bearing rocks (Rajesh et al., 2013). The host fine- to medium-grained, tonalitic, biotite-amphibole Sand River orthogneiss from the traverse section contains no pyroxene, with K-feldspar observed in the rock only as inclusions in plagioclase, presumably exsolved from high-temperature feldspar solid solution upon cooling (Figures 2a and b). The texturally and mineralogically similar partially dehydrated Sand River gneiss shows local occurrence of intergranular K-feldspar microveins accompanied by clinopyroxene and orthopyroxene developing after biotite and/or amphibole (Figure 2c).

Figure 1. *(**a**) Geologic map of the area around Musina on a Landsat TM742 (as RGB) satellite image showing the Causeway locality. The TM742 band combination uses false colors to separate soil and different lithologies from vegetation and water (see online version of the article for the colors). The regions appearing in shades of brown (earthy tone) and labeled Sand River gneiss in the image include migmatitic gneissic rocks of the Sand River gneiss interlayered with migmatitic metapelitic gneisses of the Beit Bridge Complex (BBC); mafic to ultramafic rocks of the Musina layered intrusion appear in shades of violet; quartzites of the BBC forms ridges and appear in shades of green. (**b**) TM742 compilation for southern Africa showing the location of Limpopo Complex with respect to the Kaapvaal Craton to the south and the Zimbabwe Craton to the north. The approximate extents of the three subzones of the Limpopo Complex are indicated by SMZ (Southern Marginal Zone), CZ (Central Zone) and NMZ (Northern Marginal Zone). The white box indicates the area covered in (a). (**c**) Field photograph illustrating the representative Sand River gneiss traverse section exposed at the Causeway locality. The present study focuses on the tonalitic vein with orthopyroxene-bearing dehydration zones (highlighted by the red ellipse). The pocket knife in the image is 11 cm long.*

Similar orthopyroxene-forming reaction textures after biotite and/or amphibole (e.g., Bt+Qz→Opx+Kfs+H_2O) are preserved in the adjacent pyroxene-bearing domains. The modal percentage of major ferromagnesian minerals (orthopyroxene/biotite/ amphibole) in these rocks is as follows: 0/19/13 in the initial gneiss, 4/12/10 in the partially dehydrated gneiss, 9/7/4 in the dehydrated transition zone, and 11/5/3 in the tonalitic veins. Higher modal abundance as well as size of orthopyroxene, and lesser abundance of amphibole and biotite in the tonalitic veins relative to the adjacent pyroxene-bearing domains, support the progression of dehydration of the pyroxene-absent Sand River orthogneiss (Figures 2a to 2g). Studies of fluid inclusions in quartz from the dehydrated rocks indicate the presence of a fluid with CO_2, NaCl and H_2O components (e.g., Figure 2h), with higher salinity of the fluid (up to 29% NaCl) in the orthopyroxene-bearing patches within the tonalitic veins relative to the dehydrated transition zone. The increase in Cl content in biotite, amphibole and fluorapatite from the Sand River orthogneiss to the orthopyroxene-bearing patches (Figures 2i, j and k) supports the presence of a Cl-rich brine fraction in the fluid responsible for the dehydration process.

Timing of events

Short-prismatic, euhedral zircons with no rounded terminations from an orthopyroxene-bearing melt patch within the Sand River gneiss from the Causeway locality gave a U-Pb isotope dilution thermal ionization mass spectrometry age of 2006 ± 8 Ma (Jaeckel et al., 1997). Significantly, the melt patch sample studied by Jaeckel et al. (1997) also contains a second population of long-prismatic and rounded zircon grains which gave a Pb-Pb evaporation age of 2324.0 ± 0.3 Ma. This age was interpreted as a xenocrystic age inherited from the original Sand River gneiss from which the melt patch was derived by anatexis (Jaeckel et al., 1997).

Zeh et al. (2007) reported U-Pb zircon ages on a grey banded tonalitic Sand River gneiss that is truncated and cut by numerous later melt batches. The sample (sample SR), collected from the bed of the Sand River near the Causeway locality, consists of plagioclase, quartz, biotite, minor hornblende, and orthopyroxene. Zircon cores yielded concordant ages of 3283 ± 3 Ma and of 3143 ± 13 Ma, whereas zircon overgrowths and structureless zircon grains gave concordant ages of 2614 ± 11 Ma and 2014 ± 10 Ma (Zeh et al., 2007). These authors correlate the youngest age to the Palaeoproterozic granulite-facies metamorphic overprint. Gerdes and Zeh (2009) reported a similar age pattern from a grey banded tonalitic gneiss (sample SR; sampling co-ordinates given in both studies are same) with similar mineralogy (with minor orthopyroxene) from the bed of the Sand River near the Causeway locality (3281 ± 7.5 Ma, 3143 ± 14 Ma, 2664 ± 16 Ma, 2021 ± 10 Ma). Zeh et al. (2010) reported U-Pb zircon ages from three orthopyroxene-bearing tonalitic gneissic samples from the bed of the Sand River near the Causeway locality. Although the three samples contain minor orthopyroxene and gave similar protolith ages (sample SR6R to 3268 ± 8 Ma, SR6Rb to 3267 ± 11 Ma, SR6Ra to 3274 ± 7 Ma), only one sample (SR6Ra) gave a Paleoproterozoic (2024 ± 8 Ma) zircon overgrowth age, while SR6Rb recorded a zircon overgrowth age of 2660 ± 97 Ma and no overgrowth ages were reported for SR6R (Zeh et al., 2010). Interestingly, the lower $^{176}Lu/^{177}Hf$ ratio of the ~2.02 Ga zircon overgrowths in the tonalitic gneiss samples studied by Gerdes and Zeh (2009) and Zeh et al. (2010) was interpreted by the respective authors to indicate that Lu fractionated into orthopyroxene, which occurs in small quantities in the gneiss samples and may have formed during anatexis of the Sand River gneiss. Zeh et al. (2010) also reported a U-Pb zircon emplacement age of 2021 ± 6 Ma for a tonalitic leucosome. But the field photograph and petrographic details given in Zeh et al. (2010) are typical of that of biotite-bearing granite pegmatite, similar to those for a 2003 ± 11 Ma granite pegmatite reported by Jaeckel et al. (1997) and studied in Rajesh et al. (2013).

Considering the multiple metamorphic overgrowth ages reported from orthopyroxene-bearing tonalitic Sand River gneiss samples (Zeh et al., 2007; Gerdes and Zeh, 2009), we resorted to $^{40}Ar/^{39}Ar$ dating on amphibole from a dehydrated Sand River gneiss sample from the studied section to constrain the timing of events. Electron microprobe analyses were carried out on amphiboles in representative thin sections from the dated sample. Analytical details are given in Appendix 1, and the microprobe analytical data are given in table 1. Amphiboles in the selected sample almost always occur associated with pyroxene, and are characterized by X_{Mg} of 0.48 to 0.51, and Al_2O_3 and TiO_2 contents of 9.81 to 11.38 weight % and 1.46 to 2.12 weight %, respectively (Figures 3a and b; Table 1). The composition is similar to those of amphibole inclusions (X_{Mg} – 0.48 to 0.54; Al_2O_3 – 10.22 to 11.35 weight %; TiO_2 – 1.21 to 1.47 weight %; Figures 3a and b; Table 1) occurring within large orthopyroxene grains in tonalitic veins (e.g., Figure 2f). Significantly, amphiboles replacing orthopyroxene (e.g., Figure 2g) from the dehydrated transition zone have quite different composition (X_{Mg} – 0.71; Al_2O_3 – 2.41 to 3.32 weight %; TiO_2 – 0.12 to 0.23 weight %; Figures 3a and b; Table 1).

Methods used for $^{40}Ar/^{39}Ar$ dating are described in Appendix 1, with the value for the ^{40}K decay constant adopted from Renne et al. (2010). The Ar analytical results for the studied sample, including Ca/K and Cl/K ratios, are listed in Table 2. The amphibole from the dehydrated Sand River gneiss yielded a plateau age of 2037±10 Ma (Figure 3c). The Ca/K ratios of the ~2.0 Ga amphibole (6.7 to 7.9; Table 2), derived from $^{37}Ar/^{39}Ar$ ratios, are in good agreement with those obtained for amphiboles by electron microprobe (~6.8 to 7.4; Figures 3a and b; Table 1). The Ca/K ratios of amphiboles found as inclusions in orthopyroxene from the tonalitic vein (~7.1 to 7.8; Figures 3a and b; Table 1) are also similar to the ones dated by $^{40}Ar/^{39}Ar$ method.

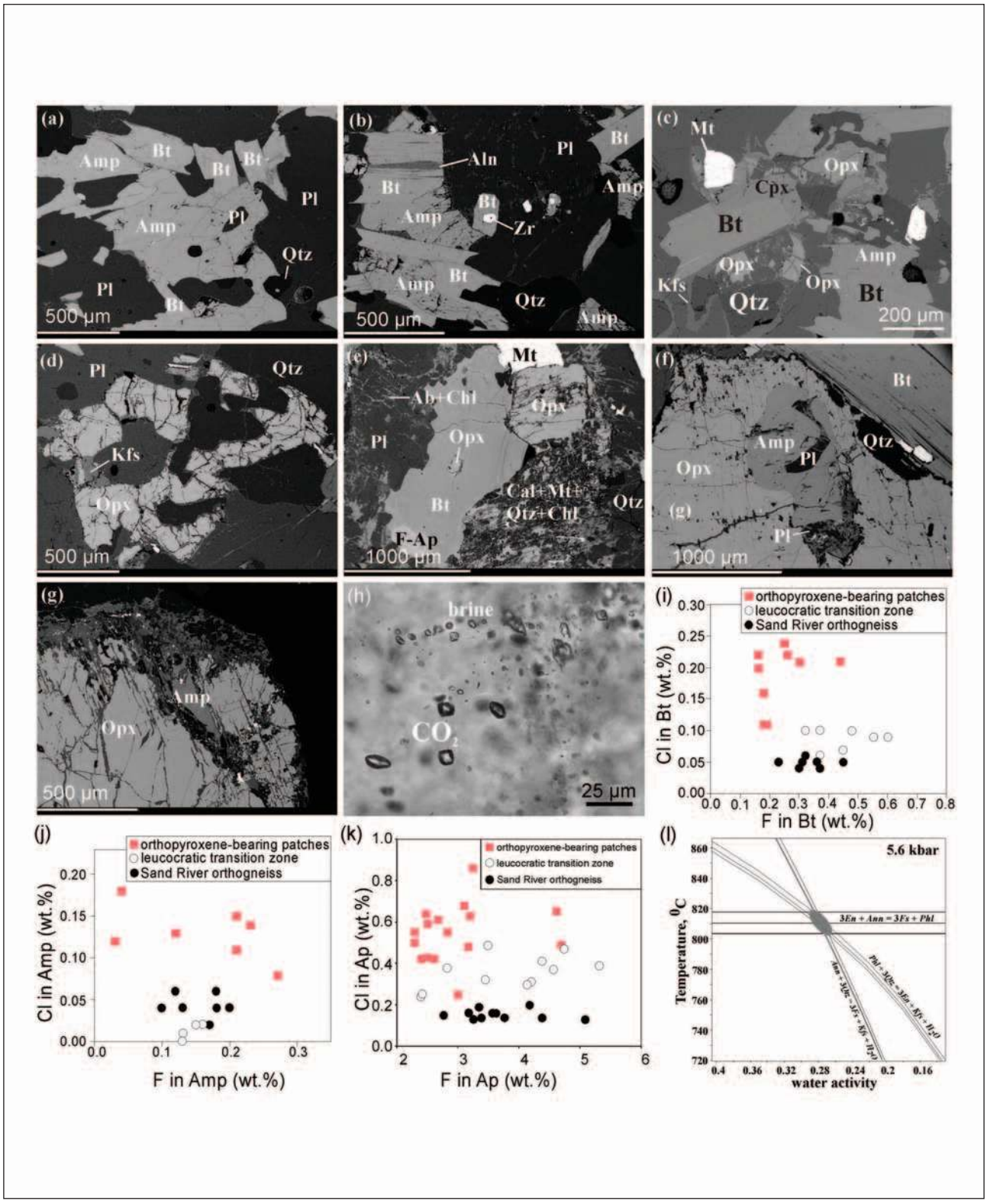

Figure 2. *Evidence for fluid-induced dehydration of the pyroxene-absent Sand River gneiss [compiled from Safonov et al. (2012) and Rajesh et al. (2013)]. Representative back scattered electron (BSE) images from pyroxene-absent Sand River gneiss (**a**, **b**), dehydrated Sand River gneiss rocks (**c**, **d**) and tonalitic vein with orthopyroxene-bearing dehydration zones (**e**, **f**, **g**). Amp – amphibole; Pl – plagioclase; Qtz – quartz; Kfs – K-feldspar; Opx – orthopyroxene; Bt – biotite; Cpx – clinopyroxene; F-Ap – fluorapatite; Cal – calcite; Chl – chlorite; Ab – albite; Mt – magnetite; Aln – Allanite; Zr - Zircon. Brine and CO_2-rich fluid inclusions in quartz from the tonalitic vein with dehydration zones (**h**). Variation in Cl and F contents in biotite (**i**), amphibole (**j**) and apatite (**k**) respectively from the three adjacent zones. Water activity values calculated using winTWQ 2.3 software for orthopyroxene and biotite associated with K-feldspar and quartz in the orthopyroxene-bearing tonalitic vein (**l**). The calculation was carried out for 5·6 kbar.*

Table 1. Representative mineral chemical data of amphiboles associated with orthopyroxene from the dehydrated Sand River gneiss (GAB-7 sample) used for $^{40}Ar/^{39}Ar$ dating, compared with those occurring as inclusions in orthopyroxene from the tonalitic vein (GAB-6 sample) and amphiboles replacing orthopyroxene from the dehydrated transition zone (GAB-8 sample).

	GAB-7*	GAB-7*	GAB-7*	GAB-7*	GAB-7*	GAB-7*	GAB-7*	GAB-7*	GAB-7*	GAB-7*	GAB-7**	GAB-7**	GAB-7**	GAB-6*	GAB-6**	GAB-6*	GAB-6*	GAB-6*	GAB-6*	GAB-6*	GAB-6*	GAB-8*	GAB-8*	GAB-8**
SiO_2	41.87	42.44	42.56	42.65	43.23	42.52	43.23	42.52	42.59	41.66	41.74	43.07	42.15	42.51	41.74	43.23	43.91	43.56	43.34	43.14	43.46	51.86	53.99	54.01
TiO_2	1.79	2.12	2.01	1.89	1.73	1.92	1.73	1.92	1.46	1.55	1.88	1.63	1.99	1.28	1.47	1.31	1.45	1.29	1.45	1.21	1.40	0.23	0.17	0.12
Al_2O_3	9.81	10.21	10.08	10.28	11.09	10.84	11.09	10.84	10.50	11.38	9.96	10.15	9.87	10.28	10.61	11.35	10.54	11.25	10.81	11.44	10.35	3.32	2.56	2.41
Cr_2O_3	0.03	0.03	0.02	0.04	0.00	0.00	0.00	0.00	0.00	0.00	0.05	0.01	0.05	0.04	0.04	0.00	0.00	0.00	0.00	0.00	0.00	0.02	0.02	0.00
FeO	17.97	18.14	18.40	18.14	17.93	18.51	17.93	18.51	17.55	18.77	18.38	18.06	18.28	17.41	18.58	16.49	16.43	17.12	17.83	17.97	18.64	11.92	12.07	12.08
MnO	0.34	0.40	0.40	0.44	0.28	0.50	0.28	0.50	0.40	0.40	0.44	0.42	0.42	0.38	0.50	0.42	0.68	0.43	0.59	0.64	0.67	0.62	0.66	0.68
MgO	9.67	9.51	9.49	9.54	10.37	9.96	10.37	9.96	10.37	9.70	9.54	9.65	9.67	10.32	9.80	10.82	11.13	10.56	10.52	10.11	10.53	16.20	16.47	16.72
CaO	11.61	11.34	11.53	11.69	11.58	11.35	11.58	11.35	11.24	11.33	11.49	11.60	11.40	11.08	11.25	11.32	10.62	11.29	10.76	11.40	10.80	11.63	11.72	11.84
Na_2O	1.31	1.40	1.33	1.32	1.23	1.45	1.23	1.45	1.17	1.39	1.39	1.06	1.35	1.53	1.44	1.22	1.34	1.01	1.19	1.11	1.27	0.19	0.13	0.15
K_2O	1.37	1.39	1.33	1.40	1.35	1.39	1.35	1.39	1.21	1.39	1.33	1.31	1.38	1.20	1.32	1.28	1.14	1.23	1.17	1.34	1.16	0.19	0.18	0.13
Cl	0.06	0.06	0.04	0.04	n.d.	n.d.	n.d.	n.d.	n.d.	n.d.	0.04	0.02	0.04	0.18	0.15	n.d.	n.d.	n.d.	n.d.	n.d.	n.d.	0.02	0.02	0.02
F	0.18	0.12	0.10	0.13	n.d.	n.d.	n.d.	n.d.	n.d.	n.d.	0.18	0.17	0.20	0.04	0.21	n.d.	n.d.	n.d.	n.d.	n.d.	n.d.	0.16	0.16	0.15
Total	96.01	97.16	97.29	97.56	98.78	98.44	98.78	98.44	96.48	97.56	96.42	97.15	96.80	96.25	97.11	97.44	97.23	97.75	97.67	98.36	98.28	96.36	98.15	98.31
O	23	23	23	23	23	23	23	23	23	23	23	23	23	23	23							23	23	23
Si	6.501	6.497	6.511	6.504	6.464	6.422	6.464	6.422	6.514	6.362	6.467	6.574	6.495	6.538	6.428	6.503	6.604	6.538	6.536	6.480	6.545	7.580	7.723	7.717
Ti	0.209	0.244	0.231	0.217	0.194	0.218	0.194	0.218	0.169	0.178	0.219	0.187	0.231	0.148	0.170	0.148	0.164	0.146	0.165	0.137	0.158	0.025	0.018	0.013
Al(4)	1.499	1.503	1.489	1.496	1.536	1.578	1.536	1.578	1.486	1.638	1.533	1.426	1.505	1.462	1.572	1.497	1.396	1.462	1.464	1.520	1.455	0.420	0.277	0.283
Al(6)	0.297	0.340	0.328	0.351	0.418	0.351	0.418	0.351	0.408	0.409	0.286	0.400	0.287	0.401	0.353	0.515	0.471	0.529	0.457	0.506	0.383	0.151	0.155	0.123
Cr	0.004	0.004	0.002	0.005	0.000	0.000	0.000	0.000	0.000	0.000	0.006	0.001	0.006	0.005	0.005	0.000	0.000	0.000	0.000	0.000	0.000	0.002	0.002	0.000
Fe(iii)	0.000	0.000	0.000	0.000	0.000	0.000	0.000	0.000	0.000	0.000	0.000	0.000	0.000	0.000	0.000	0.000	0.000	0.000	0.000	0.000	0.000	0.000	0.000	0.000
Fe(ii)	2.333	2.322	2.354	2.313	2.242	2.338	2.242	2.338	2.244	2.396	2.381	2.305	2.355	2.239	2.393	2.075	2.066	2.149	2.249	2.258	2.347	1.457	1.444	1.443
Mn	0.045	0.052	0.052	0.057	0.035	0.064	0.035	0.064	0.052	0.052	0.058	0.054	0.055	0.049	0.065	0.053	0.086	0.055	0.076	0.081	0.086	0.077	0.080	0.082
Mg	2.239	2.171	2.164	2.169	2.312	2.242	2.312	2.242	2.364	2.207	2.204	2.196	2.221	2.366	2.250	2.427	2.495	2.362	2.366	2.263	2.365	3.530	3.512	3.561
Ca	1.931	1.860	1.890	1.910	1.855	1.836	1.855	1.836	1.842	1.853	1.907	1.897	1.882	1.826	1.856	1.824	1.711	1.815	1.739	1.835	1.742	1.821	1.796	1.812
Na	0.394	0.416	0.394	0.390	0.357	0.425	0.357	0.425	0.347	0.412	0.418	0.314	0.403	0.456	0.430	0.357	0.390	0.294	0.349	0.324	0.370	0.054	0.036	0.042
K	0.271	0.271	0.260	0.272	0.258	0.268	0.258	0.268	0.235	0.271	0.263	0.255	0.271	0.235	0.259	0.245	0.218	0.235	0.224	0.256	0.223	0.035	0.033	0.024
Total	15.723	15.679	15.675	15.684	15.672	15.741	15.672	15.741	15.661	15.778	15.742	15.609	15.711	15.726	15.781	15.644	15.602	15.585	15.625	15.660	15.674	15.153	15.076	15.100
XM_g	0.490	0.483	0.479	0.484	0.508	0.490	0.508	0.490	0.513	0.480	0.481	0.488	0.485	0.514	0.485	0.539	0.547	0.524	0.513	0.501	0.502	0.708	0.709	0.712
Ca/K	7.12	6.85	7.28	7.01	7.19	6.86	7.19	6.86	7.83	6.85	7.25	7.44	6.94	7.75	7.17	7.43	7.85	7.72	7.75	7.17	7.80	51.41	54.68	75.50

* this study; ** from Rajesh et al. (2013); n.d. – not determined

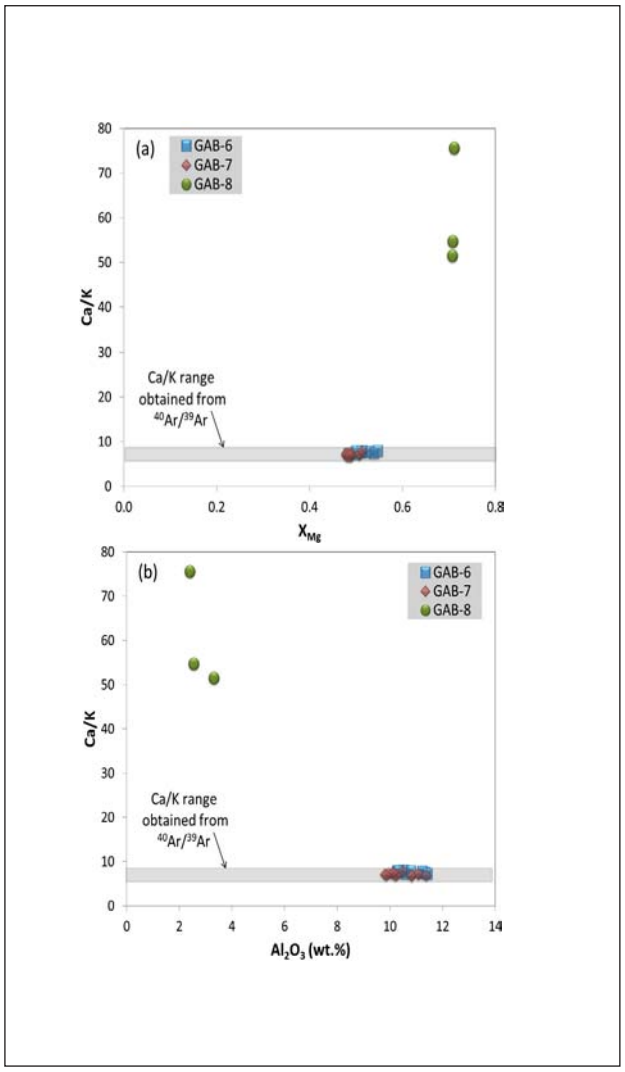

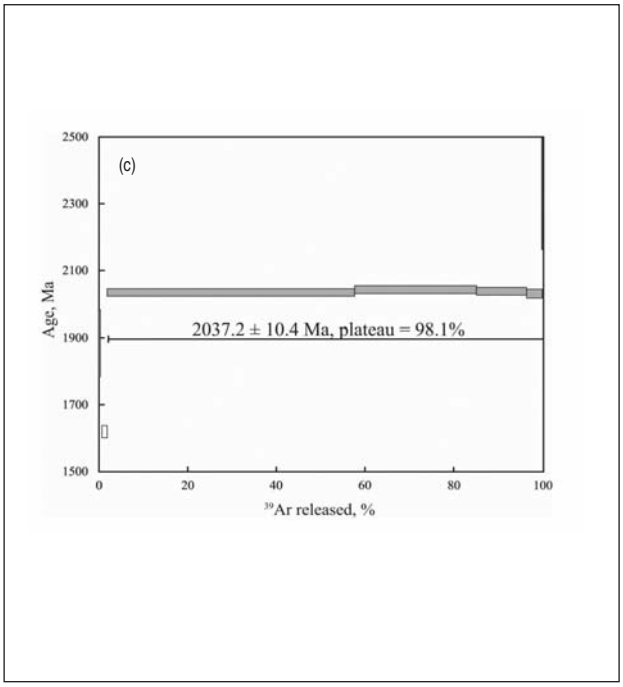

Figure 3. *Ca/K versus X_{Mg} (**a**) and Al_2O_3 (**b**) of amphiboles from the different Sand River gneiss rocks. Analyses from GAB-7 sample were obtained on amphiboles associated with orthopyroxene. Amphibole grain dated by $^{40}Ar/^{39}Ar$ was separated from the same GAB-7 sample. Analyses from GAB-6 sample (from orthopyroxene-bearing domain of the tonalitic vein) were obtained on amphibole inclusions in orthopyroxene. Analyses from GAB-8 sample were obtained from secondary amphibole replacing orthopyroxene. (**c**) $^{40}Ar/^{39}Ar$ age spectra obtained for an amphibole grain from the dehydrated Sand River gneiss (GAB-7 sample).*

On the other hand, the Ca/K ratios of secondary amphiboles replacing orthopyroxene are very high (~51 to 75; Figures 3a and b; Table 1). Thus, we interpret the ~2.04 Ga $^{40}Ar/^{39}Ar$ age to constrain the timing of fluid-induced dehydration in the Sand River gneiss studied here. Together with the ~2.01 Ga obtained by Jaeckel et al. (1997) on short-prismatic, euhedral zircons from an orthopyroxene-bearing melt patch from the Causeway locality, we constrain the timing of melting accompanying fluid-induced dehydration to the Paleoproterozoic (~2.04 to 2.01 Ga) tectono-metamorphic event that affected the Sand River gneiss.

Field and petrographic characteristics of the tonalitic vein

The tonalitic vein with dehydration zones marks a discrete ductile shear with the gneissic foliation sigmoidally transposed to the new direction bounded by shear planes (Figure 1c). The vein is built of two types of domains – orthopyroxene-bearing and orthopyroxene-absent domains – which grade from center to the margin, and are different both in mineral assemblages and textures (Figures 1c and 4). The central domain consists of large (up to 1 cm) subhedral greenish-brown orthopyroxene crystals in a coarse-grained quartz-

Table 2. $^{40}Ar/^{39}Ar$ age spectrum obtained for a single amphibole grain from the dehydrated Sand River gneiss (GAB-7 sample).

Temp. (°C)	cc stp ^{39}Ar	% ^{39}Ar	Included	Age (Ma) ± 95%	Ca/K ± 95%	Cl/K ± 95%
500	5.76566E-13	0.10	no	4138.6 ± 119.4	2.8 ± 0.8	0.0387 ± 0.0045
610	5.86412E-13	0.11	no	1882.9 ± 98.8	0.6 ± 0.7	0.0158 ± 0.0039
720	2.48364E-12	0.45	no	1194.7 ± 35.4	5.1 ± 0.2	0.0062 ± 0.0010
830	6.56412E-12	1.19	no	1619.6 ± 18.3	6.1 ± 0.1	0.0197 ± 0.0010
940	3.06669E-10	55.81	yes	2034.6 ± 11.2	6.7 ± 0.05	0.0338 ± 0.0012
1050	1.50914E-10	27.46	yes	2043.3 ± 11.8	6.7 ± 0.1	0.0339 ± 0.0012
1160	6.21723E-11	11.31	yes	2038.1 ± 11.8	7.7 ± 0.1	0.0355 ± 0.0013
1270	1.92847E-11	3.51	yes	2030.9 ± 13.3	7.9 ± 0.1	0.0418 ± 0.0016
1400	2.71325E-13	0.05	no	2394.7 ± 231.6	0	0.0229 ± 0.0076

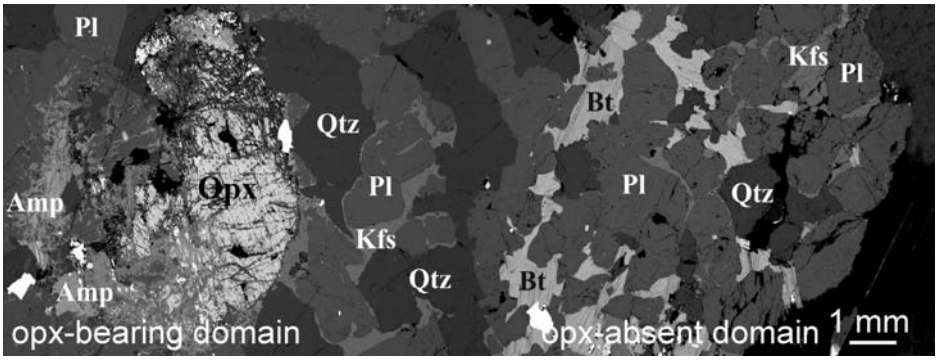

Figure 4. *Representative BSE image illustrating the transition from orthopyroxene-bearing dehydrated domain to orthopyroxene-absent melt-bearing domain of the tonalitic vein.*

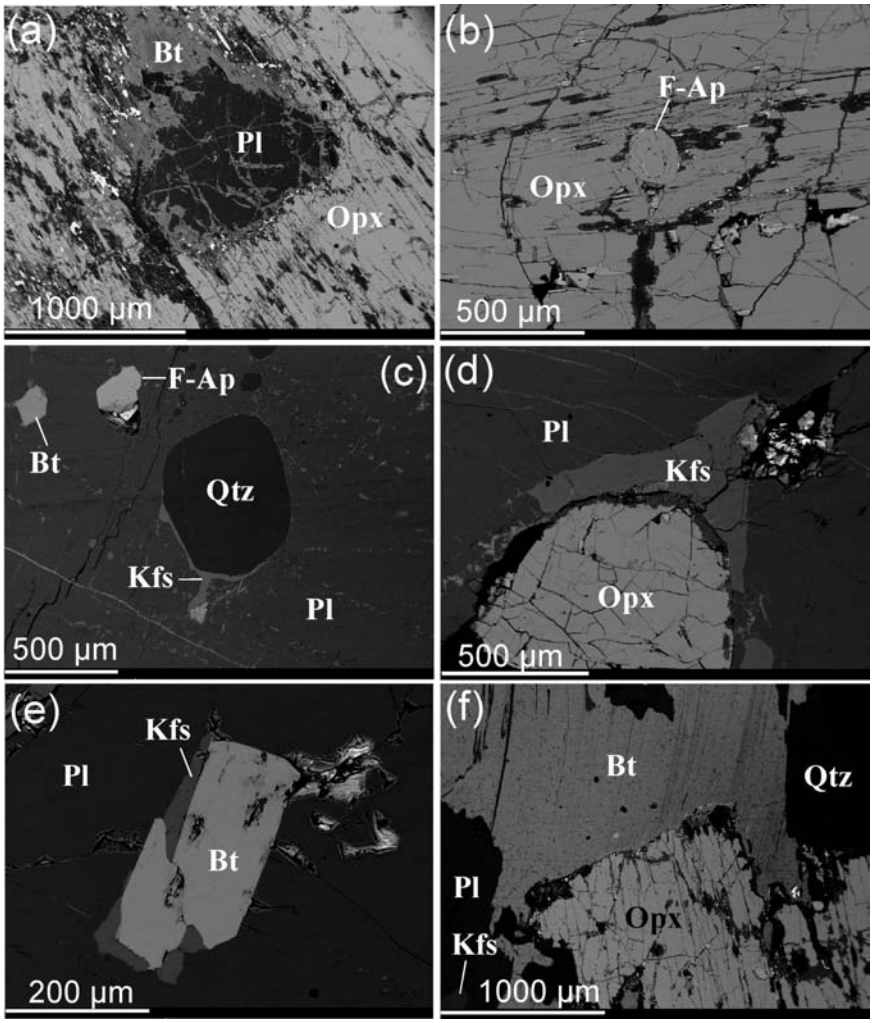

Figure 5. *Representative BSE images illustrating the variation in mineral assemblages and textures in samples from the orthopyroxene-bearing (**a** to **i**) and orthopyroxene-absent (**j** to **l**) domains of the tonalitic vein. See text for details.*

feldspar matrix. Orthopyroxene grains contain inclusions of plagioclase, amphibole, quartz, biotite and fluorapatite (Figures 2e, f, 5a and b). K-feldspar microveins are prominent along quartz-plagioclase grain boundaries (Figure 5c) and postdate the formation of orthopyroxene (Figure 5d). Biotite forms either rare inclusions in plagioclase and orthopyroxene (Figures 2e, 5c and e), or forms secondary flakes on orthopyroxene (Figure 5f). Late biotite + quartz and amphibole replace orthopyroxene, with K-feldspar occurring as part of the reaction texture (Figures 5g and h). Orthopyroxene grains are altered to chlorite-magnetite-calcite-cummingtonite aggregates, while albite-chlorite veins replace plagioclase adjacent to altered orthopyroxene (Figures 5g, h and i). Away from the orthopyroxene-bearing domain, K-feldspar veins become coarser, enveloping large euhedral to subhedral crystals of plagioclase and anhedral quartz, forming a magmatic texture (Figure 5j). Myrmekites are locally developed along the contact of plagioclase with K-feldspar (Figures 5k and l). The magmatic texture continues into the orthopyroxene-absent domain. These tonalitic domains contain biotite, forming large grains along plagioclase and quartz grain boundaries (Figure 4).

Monazite and fluorapatite characteristics

The modal per cent of fluorapatite varies from ~0.5 to 2% in the Sand River orthogneiss to ~1.5 to 5% in the tonalitic vein with dehydration zones. The size of the fluorapatite grains is also larger in the tonalitic vein with dehydration zones compared with the Sand River orthogneiss. In the tonalitic vein, fluorapatite grains dominantly occur as inclusions in plagioclase, orthopyroxene or zircon (Figures 6a, b and c). Electron

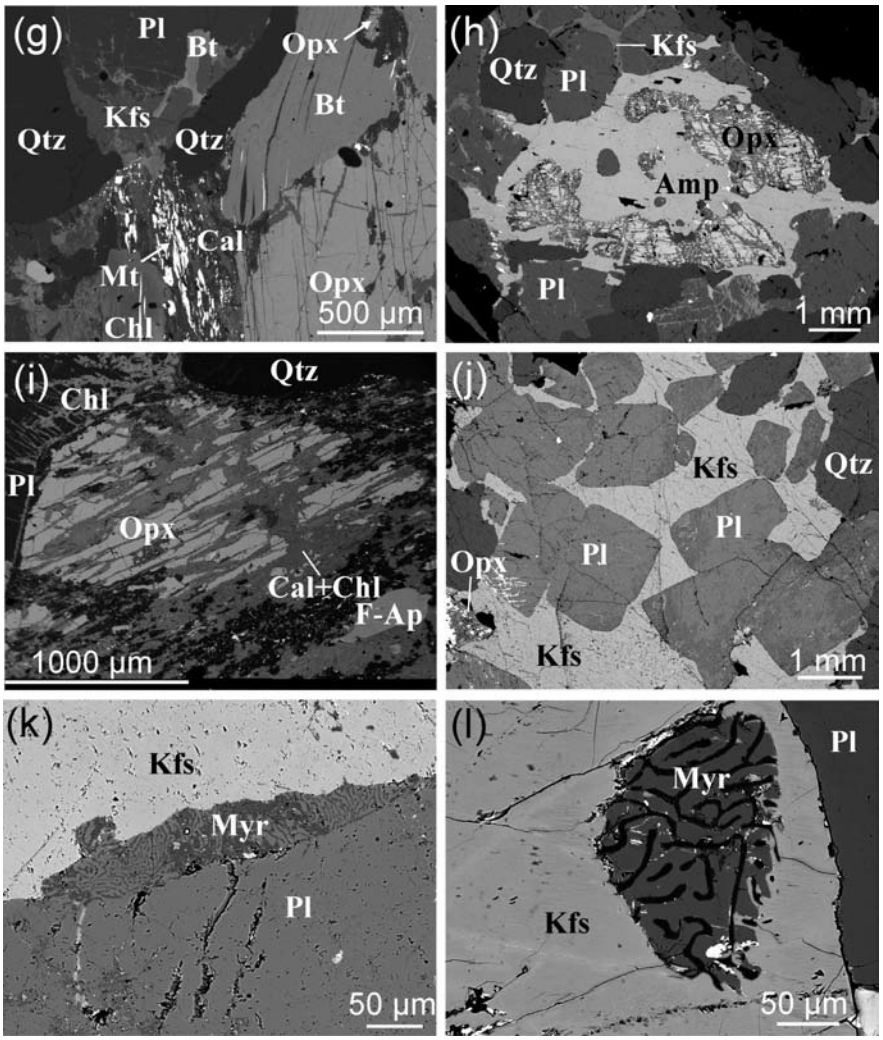

Figure 5. *continued.*

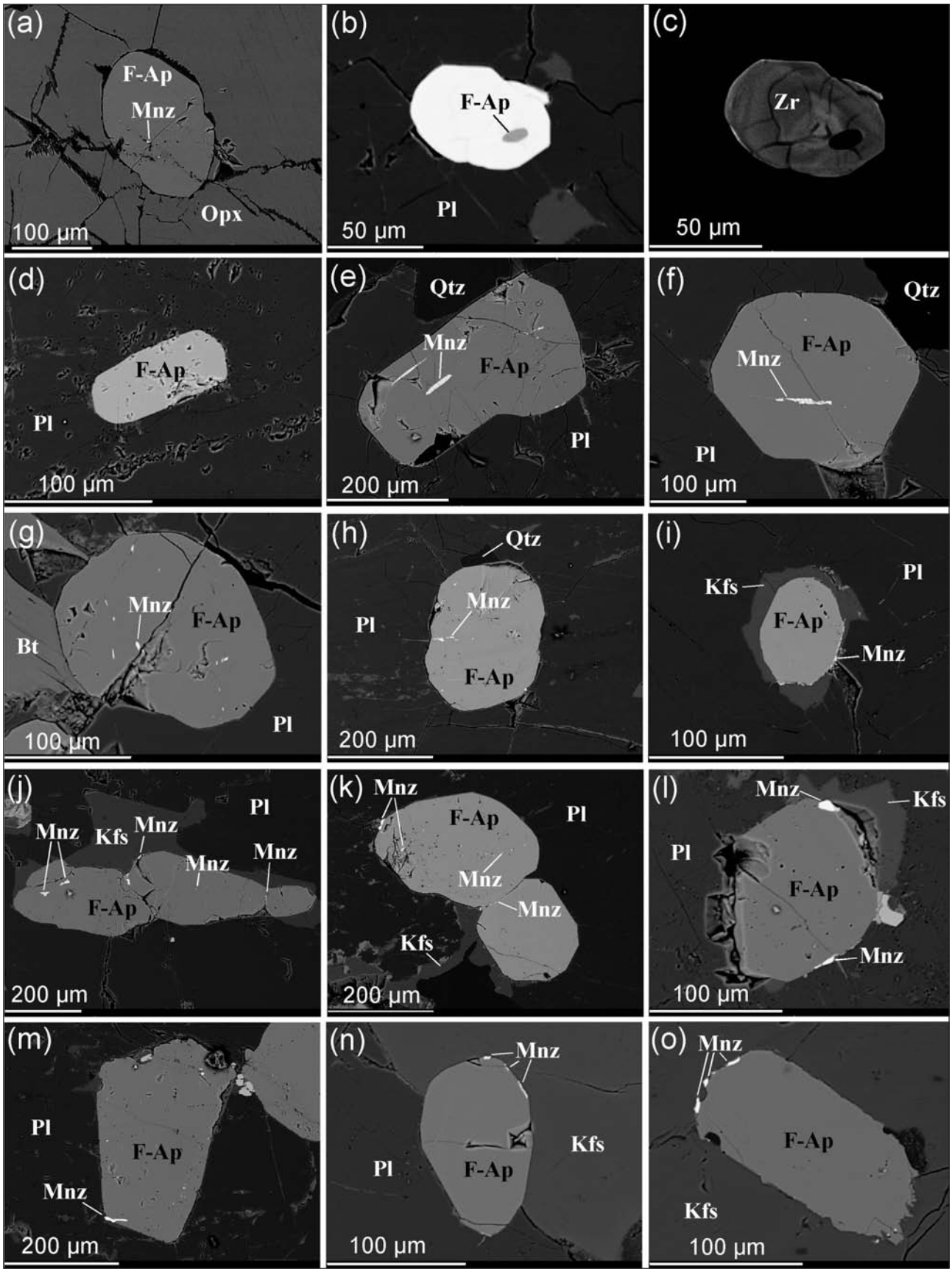

Figure 6. *Representative BSE images illustrating the typical occurrence of fluorpatite (**a** to **c**) and the variation in the association of monazite with fluorapatite as one moves from the orthopyroxene-bearing domain to the orthopyroxene-absent domain in the tonalitic vein (**e** to **o**). The typical occurrence of fluorapatite not associated with monazite in the Sand River orthogneiss is illustrated in (**d**). Mnz – monazite.*

microprobe analyses were carried out on fluorapatite grains in representative samples from the tonalitic vein (Table 3; see analytical details in Appendix 1). While the F content of fluorapatite is similar (~2.5 to 5 weight %), the Cl content is higher in the fluorapatites from the tonalitic vein with dehydration zones (~0.4 to 0.9 weight %) compared to the Sand River orthogneiss (~0.1 to 0.2 weight %) (Figure 2k; Table 3). Fluorapatites from the orthopyroxene-absent domain have higher F content than those in the orthopyroxene-bearing domain. Fluorapatite inclusions in orthopyroxene have lower F and Cl contents that those occurring in the matrix (e.g., analyses from adjacent portion – inclusion: F = 2.51 weight %; Cl = 0.43 weight %; matrix: F = 3.1 weight %; Cl = 0.68 weight %).

No monazite inclusions or rims were observed associated with fluorapatite in the host Sand River gneiss (Figure 6d). In contrast, monazite occurs as prominent inclusions in fluorapatite from the orthopyroxene-bearing domain of the tonalitic veins (Figures 6e, f, g and h). The monazite inclusions are commonly elongated parallel to the *c-axis* of the fluorapatite grains (Figure 6e). None of the fluorapatite occurring as inclusions in orthopyroxene preserves any monazite rim grains (e.g., Figure 6a). In the orthopyroxene-absent domain, monazite forms irregular rims around fluorapatite (Figures 6i to o). Near the orthopyroxene-bearing domain, K-feldspar veins occur along fluorapatite grain margins, while away from this domain K-feldspar forms large grains in a magmatic texture. In the transition zone, monazite is sporadically found both as inclusions and prominent irregular rims around fluorpatite (Figure 7a). Closer BSE inspection of the fluorapatite grain margins revealed that the monazite rims were formed later with respect to the monazite inclusions (Figure 7b). Myrmekites are commonly seen associated with the monazite rims (Figures 7a, b). Locally, the monazite rims are altered to allanite (Figures 7a and c), with allanite occasionally forming thin elongated grains filling cracks and cutting across monazite rims (Figures 7b and d).

The microprobe analytical data on monazite inclusions and rims from representative samples of the tonalitic vein are given in table 4. CaO content of monazite rims exhibits a wider range (~0.5 to 4 weight %) relative to the rather restricted CaO content of monazite inclusions (~1 to 2 weight %; one monazite inclusion has a high CaO content of 5.6 weight %). P_2O_5 content is generally uniform between the rims (~28 to 33 weight %) and inclusions (~26 to 30 weight %). SiO_2 content is generally low (~0.09 to 0.73 weight %) for both types, with rare higher contents for both rims (~7.4 weight %) and inclusions (~3.03 weight %). The difference between monazite inclusions and rims became apparent in trace and rare-earth elements, especially in their ratios. The Y_2O_3 content is lower in the rims (~0.43 to 1.81 weight %) relative to the inclusions (~0.73 to 2.11 weight %). Th/U ratio varies from ~0.37-6.97 in rims to ~0.24 to 8.2 in inclusions.

Table 3. Representative mineral chemical data for fluorapatites from the tonalitic vein (GAB-6), compared with those from the Sand River orthogneiss (GAB-7).

	GAB-6*	**GAB-6***	**GAB-6***	**GAB-6***	**GAB-6****	**GAB-6****	**GAB-6****	**GAB-6****	**GAB-7****	**GAB-7****	**GAB-7****	**GAB-7****	**GAB-7****	**GAB-7****
CaO	53.73	56.70	56.15	57.79	57.98	55.26	56.31	55.43	56.27	55.88	55.81	55.54	57.11	57.3	56.15	55.79
Na_2O	0.08	0.07	0.12	0.05	0.06	0.12	0.11	0.04	0.03	0.06	0.03	0.06	0.05	0.03	0.04	0.02
FeO	0.28	0.17	0.18	0.08	0.06	0.23	0.27	0.13	0.19	0.1	0.05	0.04	0.12	0.03	0.03	0.08
MnO	0.15	0.14	0.14	0.20	0.22	0.13	0.12	0.11	0.13	0.16	0.09	0.04	0.06	0.11	0.09	0.07
MgO	0.01	0.00	0.02	0.02	0.02	0.01	0.02	0	0.01	0	0	0.01	0.03	0	0	0.01
P_2O_5	40.79***	40.79	40.79	40.79	40.79	40.79	40.79	40.79	40.79	40.79	40.79	40.79	40.79	40.79	40.79	40.79
SiO_2	0.26	0.24	0.24	0.33	0.18	0.2	0.17	0.27	0.23	0.22	0.09	0.1	0.04	0	0.08	0.05
Cl	0.55	0.49	0.65	0.25	0.50	0.43	0.42	0.68	0.63	0.86	0.2	0.13	0.15	0.14	0.16	0.16
F	2.83	4.69	4.62	3.00	2.29	2.51	2.61	3.1	3.2	3.25	4.17	5.08	2.76	3.38	3.57	3.17
Total	98.68	103.29	102.91	102.51	102.10	58.89	100.82	100.55	101.48	101.32	101.23	101.79	101.11	101.78	100.91	100.14
O	25	25	25	25	25	25	25	25	25	25	25	25	25	25	25	25
Ca	9.606	9.753	9.688	10.04	10.138	9.821	9.926	9.769	9.852	9.796	9.756	9.64	10.042	10.009	9.857	9.863
Na	0.026	0.022	0.037	0.016	0.019	0.039	0.035	0.013	0.01	0.019	0.009	0.019	0.016	0.009	0.013	0.006
Fe	0.039	0.023	0.024	0.011	0.008	0.032	0.037	0.018	0.026	0.014	0.007	0.005	0.016	0.004	0.004	0.011
Mn	0.021	0.019	0.019	0.027	0.03	0.018	0.017	0.015	0.018	0.022	0.012	0.005	0.008	0.015	0.012	0.01
Mg	0.002	0	0.005	0.005	0.005	0.002	0.005	0	0.002	0	0	0.002	0.007	0	0	0.002
P	5.763	5.544	5.561	5.6	5.636	5.729	5.682	5.681	5.643	5.651	5.635	5.594	5.667	5.63	5.658	5.698
Si	0.043	0.039	0.039	0.054	0.029	0.033	0.028	0.044	0.038	0.036	0.015	0.016	0.007	0	0.013	0.008
Total	15.5	15.4	15.373	15.753	15.865	15.674	15.73	15.54	15.589	15.538	15.434	15.281	15.763	15.667	15.557	15.598

* this study; ** from Rajesh et al. (2013); *** P_2O_5 is calculated after average content of P_2O_5 in fluorapatite

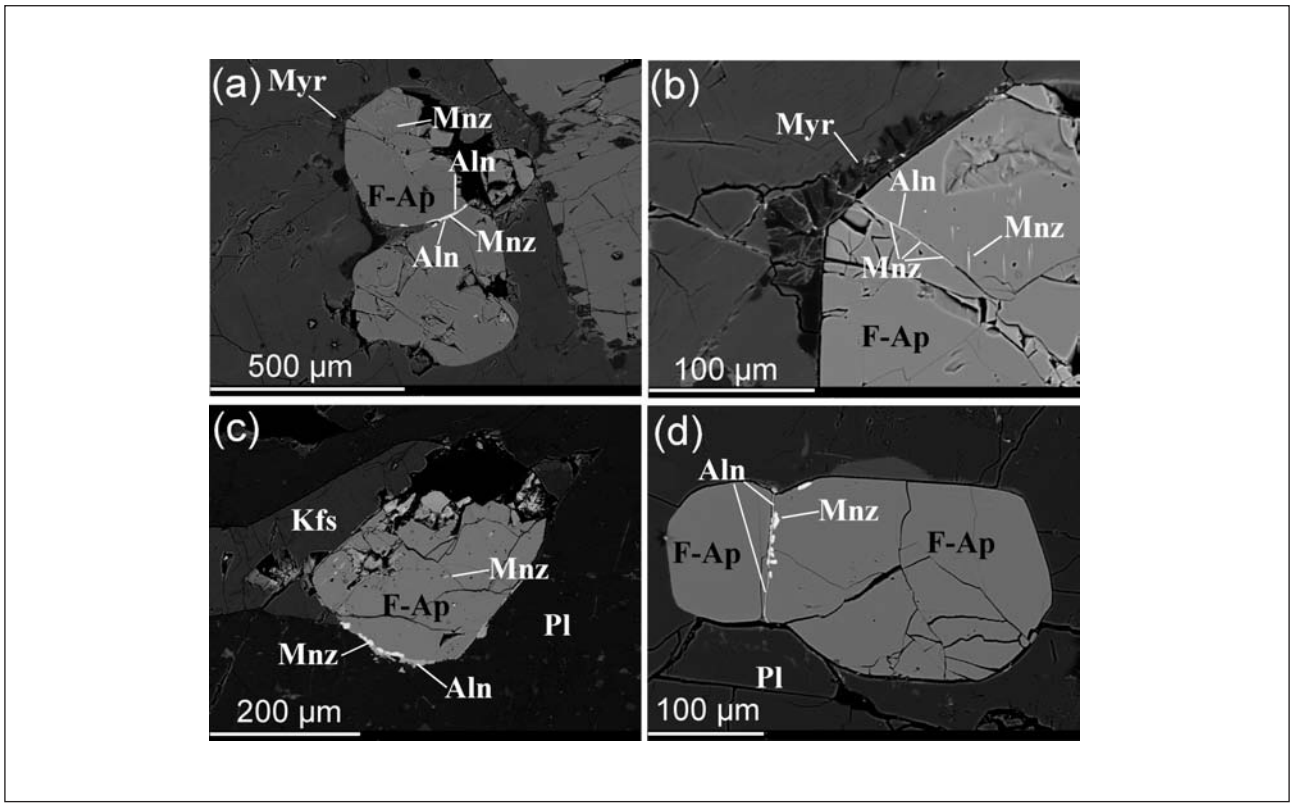

Figure 7. *Representative BSE images illustrating the occurrence of monazite as both rims and inclusions in the same fluorapatite grains (**a**, **b**, **c**). Allanite replaces monazite rims. In images such as in (**b**), minute monazite relics are seen along the length of the allanite occupying the crack in apatite. This is clearer in (**d**), where thin elongated allanite grain fill crack and postdates monazite rim grains. Myr– myrmekite.*

Sm/Nd varies from ~0.11 to 0.16 in the rims to ~0.15 to 0.18 in inclusions, while La/Sm is ~6.2 to 15.7 in the rims and ~5.1 to 7.4 in the inclusions. The Tb/Dy ratio varies from ~0.21 to 1.97 in the rims to ~0.14 to 0.55 in the inclusions. Clear distinction between the monazite rims and inclusions was observed in terms of ThO_2 and PbO versus UO_2, SmO versus La_2O_3, Sm/Nd versus Ce_2O_3, La/Sm versus Th/U, and Y_2O_3 versus HREE (Figure 8).

P-T-fluid conditions of the tonalitic vein formation

The hornblende-plagioclase-quartz thermobarometer (Schmidt, 1992; Holland and Blundy, 1994; Andersen and Smith, 1995) applied to the primary assemblage amphibole-biotite-plagioclase-quartz in the partially dehydrated gneiss gave P-T conditions of 730 to 790°C and 5.6 to 6.2 kbar (Safonov et al., 2012; Rajesh et al., 2013). Temperatures of 811 ± 6°C (Figure 2l) estimated from the composition of rare biotite and orthopyroxene in contact in the tonalitic vein are considered as the peak temperature for the dehydration and partial melting process (Safonov et al., 2012; Rajesh et al., 2013) For these temperatures, they reported water activity of 0·28 to 0·26 (Figure 2l) using compositions of biotite, orthopyroxene and K-feldspar from the tonalitic vein and the thermodynamic database of Berman and Aranovich (1996) implemented into the winTWQ software, version 2.32 (Berman, 2007). Such low water activity can hardly provoke melting of quartz-feldspar assemblages at temperatures of ~800°C (Ebadi and Johannes, 1991; Aranovich et al., 2013). It cannot be excluded that the above estimates of aH_2O are an artefact, since K-feldspar in the vein was not initially in equilibrium with orthopyroxene, biotite and melt, but was formed later, either at the final stage of the melt crystallization or metasomatically via interaction with post-magmatic saline fluid (Safonov et al., 2012). The interstitial position of K-feldspar with respect to plagioclase and orthopyroxene in the vein supports this suggestion (Figures 4, 5d, h, and j). The original water activity during formation of the orthopyroxene-bearing assemblages within the tonalitic vein could have been higher.

In order to constrain aH_2O during formation of the tonalitic vein, we computed a T-aH_2O pseudosection (Figure 9) for the bulk composition of a sample, which includes quartzo-feldspathic portion of the tonalitic vein adjacent to orthopyroxene, and presumably, closely represent the solidified melt (in weight %): SiO_2 = 73.53, Al_2O_3 = 12.89, Fe_2O_3 = 3.12, MgO = 1.16, CaO = 2.68, Na_2O = 3.36, K_2O = 1.37, TiO_2 = 0.42, P_2O_5 = 0.01, MnO = 0.05, at 5.6 kbar using the Gibbs energy minimization method implemented into the PERPLE_X software (Connolly, 2005) (version 6.7.0 for Windows with the standard properties database hp02ver.dat; http://www.perplex.ethz.ch). Mixing models for Ti-bearing biotite – Bio(TCC), orthopyroxene – Opx(HP),

Table 4. Representative mineral chemical data of monazite inclusions and rims associated with fluorapatite from the tonalitic vein (GAB-6 samples).

	inclusion	inclusion	inclusion	inclusion	inclusion	inclusion	inclusion	rim	rim	rim	rim	rim	rim	rim	rim	rim	rim	rim	rim
Al_2O_3	0.00	0.00	0.00	0.24	0.00	0.04	0.97	0.02	3.10	0.07	0.03	0.06	0.27	0.00	0.00	0.00	0.07	0.11	0.02
SiO_2	0.64	0.09	0.12	0.69	0.11	0.13	3.03	0.63	7.40	0.38	0.33	0.42	0.58	0.33	0.35	0.22	0.51	0.73	0.30
P_2O_5	30.13	30.19	29.90	27.83	30.05	30.11	26.38	29.12	27.88	30.08	29.96	29.48	30.06	29.68	30.15	30.06	30.15	32.62	29.78
Y_2O_3	1.66	1.70	1.24	1.79	1.72	0.73	2.11	0.51	0.43	1.32	1.81	0.81	1.46	0.97	1.09	1.16	1.39	1.03	1.35
La_2O_3	14.06	10.74	13.26	11.31	12.65	13.78	10.54	16.88	16.38	12.02	12.87	14.17	10.24	14.61	15.02	13.66	12.84	11.93	13.61
Ce_2O_3	28.31	26.29	31.14	27.67	30.35	32.04	26.78	31.79	30.00	28.96	30.60	31.66	26.51	31.71	31.68	31.92	31.00	29.56	32.26
Pr_2O_3	3.21	3.08	3.53	3.03	3.44	3.40	3.17	2.79	2.70	3.04	3.40	3.16	3.51	3.17	3.05	3.45	3.54	3.32	3.45
Nd_2O_3	13.11	11.77	13.63	12.19	13.77	13.33	12.32	9.86	9.15	12.32	13.23	12.26	15.92	12.10	11.95	13.14	13.40	13.01	13.12
SmO	2.44	1.97	2.08	1.86	2.32	1.86	2.07	1.13	1.04	1.76	2.08	1.62	3.81	1.59	1.62	1.81	1.98	1.82	1.87
EuO	0.56	0.61	0.64	0.55	0.64	0.64	0.53	0.51	0.48	0.48	0.63	0.62	1.45	0.57	0.53	0.57	0.62	0.61	0.58
Tb_2O_3	0.18	0.10	0.05	0.06	0.16	0.10	0.16	0.00	0.10	0.07	0.10	0.11	0.15	0.08	0.07	0.12	0.11	0.08	0.09
FeO	0.00	4.31	0.31	9.60	0.00	0.00	2.21	0.00	0.13	0.06	0.04	0.15	1.00	0.21	0.10	0.07	0.67	0.38	0.08
Dy_2O_3	0.41	0.41	0.32	0.38	0.29	0.26	0.49	0.02	0.10	0.34	0.48	0.26	0.69	0.20	0.28	0.24	0.35	0.20	0.10
Ho_2O_3	0.00	0.02	0.00	0.09	0.04	0.05	0.14	0.00	0.04	0.07	0.07	0.00	0.00	0.12	0.10	0.10	0.08	0.08	0.01
PbO	0.00	0.03	0.05	0.02	0.06	0.02	0.06	0.29	0.17	0.11	0.16	0.04	0.02	0.18	0.18	0.14	0.05	0.09	0.11
ThO_2	0.19	0.00	0.12	0.06	0.04	0.07	0.01	2.35	1.40	0.21	0.50	0.28	0.06	0.58	0.62	0.20	0.03	0.52	0.21
UO_2	0.06	0.04	0.04	0.08	0.06	0.01	0.05	0.34	0.27	0.21	0.26	0.11	0.07	0.32	0.32	0.28	0.09	0.16	0.26
CaO	1.73	5.60	1.36	1.38	1.68	1.33	1.23	0.63	1.67	4.14	0.51	2.21	1.63	0.81	0.87	0.98	2.52	4.58	0.62
Gd_2O_3	3.63	3.15	3.31	2.90	3.52	3.16	3.08	2.71	2.53	3.07	3.35	3.01	4.17	3.09	3.10	3.22	3.34	3.04	3.22
Er_2O_3	0.09	0.00	0.00	0.02	0.00	0.00	0.13	0.00	0.00	0.00	0.07	0.00	0.07	0.00	0.00	0.01	0.01	0.05	0.00
Yb_2O_3	0.11	0.06	0.04	0.10	0.14	0.00	0.15	0.04	0.14	0.11	0.07	0.04	0.07	0.06	0.07	0.05	0.03	0.09	0.11
Lu_2O_3	0.06	0.00	0.00	0.04	0.06	0.00	0.08	0.00	0.07	0.00	0.06	0.04	0.04	0.03	0.00	0.04	0.05	0.02	0.00
Total	100.57	100.17	101.14	101.89	101.09	101.04	95.69	99.62	105.19	98.82	100.60	100.50	101.79	100.41	101.15	101.43	102.85	104.04	101.15

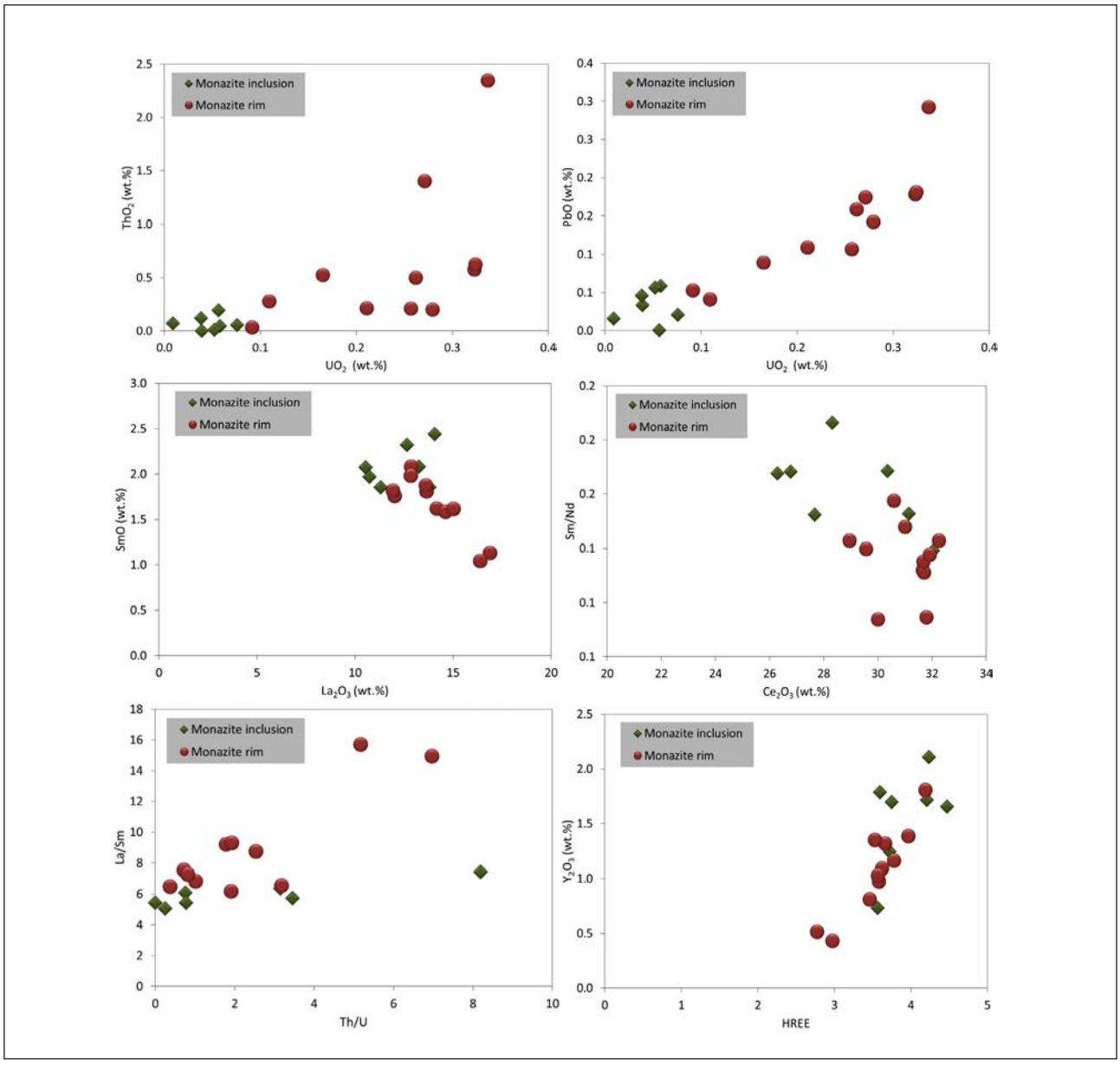

Figure 8. *Representative mineral chemical characteristics of the two types of monazite – monazite inclusions and monazite rims – associated with fluorapatite from the tonalitic vein in terms of ThO_2 versus UO_2, PbO versus UO_2, SmO versus La_2O_3, Sm/Nd versus Ce_2O_3, La/Sm versus Th/U, and Y_2O_3 versus HREE plots.*

Ca-Na-amphibole – cAmph(DP), plagioclase – Pl(h), sanidine - San, as well as for the silicate melt – melt(HP) recommended in PERPLE_X (file solution_model.dat; see http://www.perplex.ethz.ch/perplex_solution_model_glossary.html for descriptions of the models) were used in the calculations. It was assumed that the system was saturated with a fluid (i.e., a free fluid was present along with hydrous minerals and fluid-saturated melt) with the water activity indicated along the *y*-axis (Figure 9). It was also assumed that all retrograde phenomena in the orthopyroxene-bearing domains, such as late biotite and Ca-Na-amphibole formation, chloritization etc., were produced near isochemically via fluids accumulated in the melt, and do not significantly change the above bulk composition.

The pseudosection reproduces the assemblages within the tonalitic vein. The subsolidus assemblage orthopyroxene + biotite + plagioclase + quartz ± ilmenite ± sanidine is predominant over the wide T-aH_2O interval. Following the pseudosection, at temperatures of 811 ± 6°C, melt is produced at log(aH_2O) >(-0.27), i.e., aH_2O >0.54, that is significantly higher than 0.28-0.26 estimated from compositions of orthopyroxene, biotite, and K-feldspar in the vein (Safonov et al., 2012; Rajesh et al., 2013). The pseudosection shows that at aH_2O = 0.28 to 0.26 melting would begin at above 900°C, which is hardly realistic for the Sand River tonalitic gneiss and is not supported by conventional mineral thermometry. The value aH_2O >0.54 at 810°C could correspond to H_2O-CO_2 fluids with X_{H2O} > 0.42 or more aqueous

H_2O-CO_2 fluids containing (K, Na)Cl (e.g., Aranovich et al., 2010). The presence of chlorides in the fluids that participated in the formation of the tonalitic vein is supported by fluid inclusion data (Rajesh et al., 2013). Safonov et al. (2012) experimentally demonstrated that interaction of the equimolar H_2O-CO_2 fluids containing about 1 mol. % of alkali chlorides with the Sand River gneiss can produce the orthopyroxene-bearing assemblage coexisting with a granitic melt at 800°C, while at higher salt concentrations clinopyroxene becomes dominant phase.

The pseudosection (Figure 9) is in good qualitative agreement with the sequence of mineral assemblages forming in the tonalitic vein upon cooling. K-feldspar appears at the solidus only, consistent with the interstitial position of this phase within the vein. However, according to Figure 9, K-feldspar forms at the peak of the process only at $\log(aH_2O)$ below ~0.27 (aH_2O below 0.54). Decrease of temperature and/or increase of water activity destabilize K-feldspar, which reacts with orthopyroxene to form biotite. Biotite in the beginning forms via reaction of orthopyroxene with melt, and its amount increases at the expense of orthopyroxene and minor K-feldspar during cooling. At temperatures below 720°C and $\log(aH_2O)$ > -0.39 (aH_2O > 0.40), the orthopyroxene-free assemblage biotite + plagioclase + quartz + ilmenite becomes stable (Figure 9). Ca-Na-amphibole is stable below 740°C in presence of essentially water-rich (aH_2O about 1.0) fluids only (Figure 5h). This phase shows peritectic relations with biotite and orthopyroxene and coexists with melt. It is consistent with experimental results by Gardien et al. (2000), who observed formation of amphibole during H_2O-saturated melting of biotite tonalite. Thus, the analysis of the mineral assemblages in the tonalitic vein using the pseudosection allows conclusions about temporal and spatial non-uniformity of water activity during dehydration and partial melting.

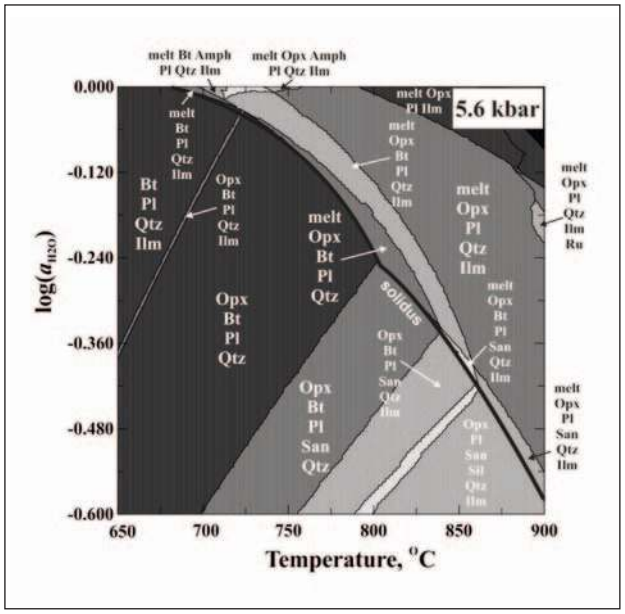

Figure 9. *T-aH_2O pseudosection computed at 5.6 kbar using the PERPLE_X software for bulk composition of the orthopyroxene-bearing domain within the tonalitic vein. Only principal phase fields are labeled. All phase fields contain free fluid phase.*

Discussion and concluding remarks

Field relations indicate that the tonalitic vein with dehydration zones represented a discrete ductile shear occupied by tonalitic melt, with orthopyroxene-bearing dehydration zones occurring in a central position along its length (Figure 1c). Orthopyroxene forming reaction textures after biotite, the low water activity prevailing during the formation of orthopyroxene (Figure 2l), the high Cl content of biotite (Figure 2i), and fluid inclusions in quartz containing dominant brine component (Figure 2h), indicate that the orthopyroxenes in the tonalitic vein are a product of dehydration by a low-aH_2O brine fluid. Prominent magmatic (interlocking texture and euhedral to subhedral grain shapes) and melt related (growth of plagioclase crystal faces against quartz) textures are preserved in the orthopyroxene-absent domain (Figures 4, 5j, k and l) (e.g., Sawyer, 1999), which surround the orthopyroxene-bearing domain. The strong alteration of the orthopyroxene-bearing domains (Figures 4, 5g, h and i) and the lack of such metasomatic alteration in the surrounding magmatic orthopyroxene-absent domains (Figures 4, 5j, k and l) indicate that melting occurred after or accompanied fluid-induced dehydration.

The progression of melting accompanying fluid-induced dehydration is further characterized by the monazite-fluorapatite characteristics in the tonalitic vein. While monazite occurs as inclusions in fluorapatite in the orthopyroxene-bearing domain (Figures 6a, e, f, g and h), it prominently occurs as irregular rims along fluorapatite grain margins in the orthopyroxene-absent domain (Figures 6i to o). Both inclusions and irregular rims were observed in the same fluorapatite grains in the transition zone (Figures 7a to c).

Experimental studies showed that the reaction of (Y+REE)-bearing fluorapatite with concentrated brine fluids results in the formation of monazite inclusions in fluorapatite via dissolution and reprecipitation (Harlov, 2012 and references therein). Such an explanation is favored for the monazite inclusions in fluorapatite in the orthopyroxene-bearing domains of the tonalitic vein. The involvement of a brine fluid is supported by fluid inclusions with salinity up to 29.2 weight % NaCl and the higher chlorine content of fluorapatite in the tonalitic vein in comparison to those in the Sand River orthogneiss (Figure 2k; Rajesh et al., 2013). K-feldspar microveins and later myrmekites are additional features indicating the participation of brines in evolution of the tonalitic vein.

As one moves from the orthopyroxene-bearing domain to the orthopyroxene-absent domain, monazite prominently occurs as rim grains around fluorapatite. Wolf and London (1995) produced small monazite

grains in glass at the margin of fluorapatite crystals by incongruent melting experiments. Such partial dissolution of fluorapatite grains to form monazite rim grains has been shown to occur in peraluminous granitic melts (e.g., Rapp and Watson, 1986; Pichavant et al., 1992; Montel, 1993; Wolf and London, 1995). In terms of whole-rock geochemical characteristics, the weakly peraluminous chemistry [ASI (molar Al/(Ca – 1.67P + Na + K) = ~1.09; molar Al/(Na + K) = ~1.84] of the melt-bearing domain of the tonalitic vein favour the incongruent dissolution of fluorapatite, with formation of monazite grains near the margins (e.g., Rapp and Watson, 1986; Montel, 1993; Wolf and London, 1995). Thus the occurrence of monazite as rims around fluorapatite is interpreted as evidence of dissolution in the presence of melt (Figures 6i to o and 7).

Monazite occurring as inclusions and rims with fluorapatite has been reported from a number of high-grade metamorphic terrains, with experimental evidence indicating that these monazite inclusions and rim grains were metasomatically induced to form from the fluorapatite (see Harlov 2012 and references therein). Unlike the high-grade rocks investigated in these different studies, characterized by no obvious evidence of partial melting (see Harlov 2012 and references therein), other studies reported the occurrence of monazite inclusions and rim grains in fluorapatite from granulite-facies rocks that have been subjected to partial melting (e.g., Harlov et al., 2007). The closest correlative to the scenario at hand is the study by Harlov et al. (2007), who related the occurrence of monazite inclusions and rim grains in fluorapatite grains from a granulite-facies metapelite to partial melting during granulite-facies metamorphism. Here, the suggestion of formation of monazite rim grains by partial dissolution of the fluorapatite in the granitic melt (Harlov et al., 2007) is similar to the results from experimental melts, which have so far shown monazite to form only as rim grains on fluorapatite (Wolf and London, 1995). On the other hand, Harlov et al. (2007) attributed the monazite inclusions in fluorapatite from the same granulite-facies metapelite to dissolution-reprecipitation of fluorapatite by aqueous fluids inherent in the granitic melt. In the present study, we relate the monazite inclusions in fluorapatite in the tonalitic leucosome to metasomatism of host fluorapatite by brine fluids. Such an argument is supported by the similarity of composition of monazite inclusions in fluorapatites from the orthopyroxene-absent domain to those in fluorapatite inclusions in orthopyroxene (with high Cl; Figure 2k). In this context, the contrasting mineral chemical characteristics observed between the monazite inclusions and rim grains associated with fluorapatite in the present study (Figure 8) are significant. Differences in behaviour of trace elements such as REE, Y, Zr, Th and U in accessory minerals between crustal melting processes under high-grade metamorphic conditions and granulite-facies metamorphism have been reported in the literature (e.g., Pan, 1997; Villaseca et al., 2003). But unlike the scenario presented here on a closely spaced domain (orthopyroxene-bearing and orthopyroxene-absent domains in a tonalitic vein), these different studies addressed the trace element behaviour of accessory minerals like monazite occurring as individual grains in granulites and migmatites from separate terranes. No direct correlatives are available. Based on the difference in textural relations of monazite inclusions and rims associated with fluorapatite, the higher Th, U and Pb contents, and lower Y, Sm and HREE contents of the monazite rims with respect to the monazite inclusions (Figure 8) are interpreted as indications that the monazite inclusions were formed during the earlier fluid-induced dehydration process, whereas the monazite rims appeared during the accompanying melting. The occurrence of allanite as overgrowths on monazite rim grains, indicate the formation of allanite after monazite rim grains due to subsoldius processes (e.g., Ward et al., 1990; Eliasson and Petersson, 1996).

Our results on monazite-fluorapatite characteristics in combination with those from Safonov et al. (2012) and Rajesh et al. (2013) make a strong case for the presence of a H_2O-CO_2-(K, Na)Cl fluid, responsible for dehydration and local partial melting of the Sand River orthogneiss, and provide an alternative view on the production of small-volume partial melts in rocks that would usually not melt at temperatures readily attainable in the Earth's crust.

Acknowledgments

University of Johannesburg and Botswana International University of Science and Technology (BIUST) are thanked for facilities. Anonymous and Armin Zeh provided detailed, encouraging and constructive comments on the manuscript. Lew Ashwal is thanked for editorial comments and efficient editorial handling. The study is supported by Russian Scientific Fund (project 14-17-00581) to OGS.

References

Anderson, J.L., Smith, D.R., 1995. The effect of temperature and oxygen fugacity on Al-in-hornblende barometry. American Mineralogist, 80, 549-59.

Aranovich L.Ya., Newton R.C., 1997. H_2O activity in concentrated KCl and KCl-NaCl solutions at high temperatures and pressures measured by the brucite-periclase equilibrium. Contributions to Mineralogy and Petrology, 127, 261-271.

Aranovich, L.Y., Newton, R.C., Manning, C.E., 2013. Brine-assisted anatexis: Experimental melting in the system haplogranite-H_2O-NaCl-KCl at deep-crustal conditions. Earth Planetary Science Letters, 374, 111-120.

Aranovich, L.Ya., Newton, R.C., 1996. H_2O activity in concentrated NaCl solutions at high pressures and temperatures measured by the brucite-periclase equilibrium. Contributions to Mineralogy and Petrology, 125, 200-212.

Aranovich, L.Ya., Zakirov, I.V., Sretenskaya, N.G., Gerya, T.V., 2010. Ternary system H_2O-CO_2-NaCl at high P-T parameters: an empirical mixing model. Geochemistry International, 48, 446-455.

Berman, R.G., 2007. WinTWQ (version 2.3): A software package for performing internally-consistent thermobarometric calculations. Geological Survey of Canada Open File 5462.

Berman, R.G., Aranovich L.Ya., 1996. Optimized standard state and solution

properties of minerals I model calibration for olivine, orthopyroxene, cordierite, garnet, and ilmenite in the system FeO-MgO-CaO-Al_2O_3-TiO_2-SiO_2. Contribution to Mineralogy and Petrology, 126, 1-24

Clarke, G.L., White, R.W., Lui, S., Fitaherbert, J.A., Pearson, N.J., 2007. Contrasting behavior of rare earth and major elements during partial melting in granulite faces migmatites, Wuluma Hills, Arunta Block, central Australia. Journal of Metamorphic Geology, 25, 1-18.

Connolly, J.A.D., 2005. Computation of phase equilibria by linear programming: A tool for geodynamic modeling and its application to subduction zone decarbonation. Earth and Planetary Science Letters, 236, 524-541.

Ebadi, A., Johannes, W., 1991. Beginning of melting and composition of first melt in the system Qz-Ab-Or-H_2O-CO_2. Contribution to Mineralogy and Petrology, 106, 286-329.

Eliasson, T., Petersson, J., 1996. Deuteric accessory phases in the Bohus granite, SW Sweden, GFF 118, Supplement 004, 12-13.

Fripp, R.E.P., 1983. The Precambrian geology of the area around the Sand River near Messina, Central Zone, Limpopo mobile belt. In: W.J. Van Biljon, and J.H. Legg, (Editors.), The Limpopo Mobile Belt. Special Publication, Geological Society of South Africa, 8, 89-102.

Gardien, V., Thompson, A.B., Ulmer, P., 2000. Melting of biotite + plagioclase + quartz gneisses: the role of H_2O in the stability of amphibole. Journal of Petrology, 41, 651-666.

Gerdes, A., Zeh, A., 2009. Zircon formation versus zircon alteration new insights from combined U-Pb and Lu-Hf *in-situ* LA-ICP-MS analyses, and consequences for the interpretation of Archaean zircon from the Central Zone of the Limpopo Belt. Chemical Geology, 261, 230-243.

Hansen, E., Stuk, M., 1993. Orthopyroxene-bearing mafic migmatites at Cone Peak, California: evidence for the formation of migmatitic granulites by anatexis in an open system. Journal of Metamorphic Geology, 11, 291-307.

Harlov, D.E., 2012. The potential role of fluids during regional granulite-facies dehydration in the lower crust. Geoscience Frontiers, 3, 813-827.

Harlov, D.E., Marschall, H.R., Hanel, M., 2007. Fluorapatite-monazite relationships in granulite-facies metapelites, Schwarzwald, southwest Germany. Mineralogical Magazine, 71(2), 223-234.

Holland, T., Blundy, J., 1994. Non-ideal interactions in calcic amphiboles and their bearing on amphibole-plagioclase thermometry. Contributions to Mineralogy and Petrology, 116, 433-47.

Jaeckel, P., Kröner, A., Kamo, S.L., Brandl, G., Wendt, J.I., 1997. Late Archaean to early Proterozoic granitoid magmatism and high-grade metamorphism in the central Limpopo belt, South Africa. Journal of the Geological Society of London, 154, 25-44.

Kramers, J.D., McCourt, S., Roering, C., Smit, C.A., Van Reenen, D.D., 2011. Tectonic models proposed for the Limpopo Complex: Mutual compatibilities and constraints. Geological Society of America Memoir, 207, 311-324.

Kröner, A., Jaeckel, P., Brandl, G., Nemchin, A.A., Pidgeon, R.T., 1999. Single zircon ages for granitoid gneisses in the Central Zone of the Limpopo Belt, Southern Africa and geodynamic significance. Precambrian Research, 93, 299-337.

Kröner, A., Jaeckel, P., Hofmann, A., Nemchin, A.A., Brandl, G., 1998. Field relationships and age of supracrustal Beit Bridge Complex and associated granitoid gneisses in the Central Zone of the Limpopo Belt, South Africa. South African Journal of Geology, 101, 201-213.

Montel, J.M., 1993. A model for monazite/melt equilibrium and application to the generation of granitic magmas. Chemical Geology, 110, 127-146.

Pan, Y., 1997. Zircon- and monazite-forming metamorphic reactions at Manitouwadge, Ontario. Canadian Mineralogist, 35, 105-118.

Pattison, D.R.M., 1991. Infiltration-driven anatexis in granulite facies metagabbro, Grenville Province, Ontario, Canada. Journal of Metamorphic Geology, 9, 315-332.

Perchuk, L.L., Safonov, O.G., Gerya, T.V., Fu, B., Harlov, D.E., 2000. Mobility of components in metasomatic transformation and partial melting of gneisses: an example from Sri Lanka. Contributions to Mineralogy and Petrology, 140, 212-232.

Pichavant, M., Montel, J.M., Richard, L.R., 1992. Apatite solubility in peraluminous liquids: Experimental data and an extension of the Harrison-Watson model. Geochimica et Cosmochimica Acta, 56, 3855-3861.

Prince, C., Harris, N.B.W., Vance, D., 2001. Fluid-enhanced melting during prograde metamorphism. Journal of the Geological Society of London, 158, 233-242.

Pyle, J.M., Spear, F.S., Wark, D.A., 2002. Electron microprobe analyses of REE in apatite, monazite and xenotime: Protocols and pitfalls. In: J.M. Kohn, J. Rakovan, J.M. Hughes (Editors) Phosphates: Geochemical, geobiological and material importance. Reviews in Mineralogy and Geochemistry, 48, 337-362.

Rajesh, H.M., Belyanin, G.A., Safonov, O.G., Kovaleva, E.I., Golunova, M.A., van Reenen, D.D., 2013. Fluid-induced dehydration of the paleoarchean Sand River biotite-hornblende gneiss, Central Zone, Limpopo Complex, South Africa. Journal of Petrology, 54, 41-74.

Rapp, R.P., Watson, E.B., 1986. Monazite solubility and dissolution kinetics: implications for the thorium and light rare earth chemistry of felsic magmas. Contributions to Mineralogy and Petrology, 94, 304-316.

Renne, P.R., Mundil, R., Balco, G., Min, K., Ludwing, K.R., 2010. Joint determination of ^{40}K decay constants and $^{40}Ar/^{40}K$ for the Fish Canyon sanidine standard, and improved accuracy for $^{40}Ar/^{39}Ar$ geochronology. Geochimica et Cosmochimica Acta, 74, 5349-5367.

Retief, E.A., Compston, W., Armstrong, R.A., Williams, I.S., 1990. Characteristics and preliminary U Pb ages of zircons from Limpopo Belt lithologies. Abstract volume, Limpopo Workshop, Rand Afrikaans University, Johannesburg, South Africa, pp. 95-99.

Safonov, O.G., Kovaleva, E.I., Kosova, S.A., Rajesh, H.M., Belyanin, G.A., Golunova, M.A., van Reenen D.D., 2012. Experimental and petrological constraints on local-scale interaction of biotite-amphibole gneiss with H_2O-CO_2-(K, Na)Cl fluids at middle-crustal conditions: Example from the Limpopo Complex, South Africa. Geoscience Frontiers, 3, 829-841.

Sawyer, E.W., 1999. Criteria for the recognition of partial melting. Physics and Chemistry of the Earth, Series A, 24, 269-279.

Schmidt, M.W., 1992. Amphibole composition in tonalite as a function of pressure: an experimental calibration of the Al-in-hornblende barometer. Contributions to Mineralogy and Petrology, 110, 304-10.

Smit, C.A., Van Reenen, D.D., Roering, C., Boshoff, R., Perchuk, L.L., 2011. Neoarchean to Paleoproterozoic evolution of the polymetamorphic Central Zone of the Limpopo Complex. Geological Society of America Memoir, 207, 213-244.

Tsunogae, T., Yurimoto, H., 1995. Single zircon U-Pb geochronology of the Limpopo Belt by secondary ion mass spectrometry. Geochemical Journal 29, 197-205.

Van Reenen, D.D., Boshoff, R., Smit, C.A., Perchuk, L.L., Kramers, J.D., McCourt, S., Armstrong, R.A., 2008. Geochronological problems related to polymetamorphism in the Limpopo Complex, South Africa. Gondwana Research, 14, 644-662.

Villaseca, C., Martín Romera, C., De la Rosa, J., Barbero, L., 2003. Residence and redistribution of REE, Y, Zr, Th and U during granulite-facies metamorphism: behaviour of accessory and major phases in peraluminous granulites of central Spain. Chemical Geology, 200, 293-323.

Ward, C.D., McArthur, J.M., Walsh, J.N., 1990. Rare earth element behavior during evolution and alteration of the Dartmoor granite, SW England. Journal of Petrology, 33, 785-815.

Waters, D.J., 1988. Partial melting and the formation of granulite facies assemblages in Namaqualand, South Africa. Journal of Metamorphic Geology, 6, 387-404.

White, R.W., Powell, R., 2002. Melt loss and the preservation of granulite facies mineral assemblages. Journal of Metamorphic Geology, 20, 621-632.

Wolf, M.B., London, D., 1995. Incongruent dissolution of REE- and Sr-rich apatite in peraluminous granitic liquids: differential apatite, monazite and xenotime solubilities during anatexis. American Mineralogist, 80, 765-775.

Zeh, A., Gerdes, A., Barton Jr., J.M., Klemd, R., 2010. U-Th-Pb and Lu-Hf systematics of zircon from TTG's, leucosomes, meta-anorthosites and quartzites of the Limpopo Belt (South Africa): Constraints for the formation, recycling and metamorphism of Palaeoarchaean crust. Precambrian Research, 179, 50-68.

Zeh, A., Gerdes, A., Klemd, R., Barton Jr., J.M., 2007. Archaean to Proterozoic crustal evolution in the Central Zone of the Limpopo Belt (South Africa/Botswana): constraints from combined U-Pb and Lu-Hf isotope analyses of zircon. Journal of Petrology, 48, 1605-1639.

Editorial handling: L.D. Ashwal.

Appendix 1: Analytical details

For $^{40}Ar/^{39}Ar$ dating, individual amphibole grain ~0.5 mm in size was irradiated at NTP radioisotopes' SAFARI1 nuclear reactor at Pelindaba, South Africa, for 20 hours in position B2W with the reactor running at 20 MW. It was analyzed by stepwise heating, using a defocused beam from a continuous Nd-YAG 1064 nm laser and the MAP 215-50 noble gas mass spectrometer, housed at the central analytical facility of the University of Johannesburg. A Johnston focused-flow electron multiplier providing excellent linearity in analog mode was used for most measurements. The amphibole standards McClure Mountains and Hb3GR were used as monitors. The value for the ^{40}K decay constant derived by Renne et al. (2010) was adopted. J-values were obtained for both these standards, as well as for the Fish Canyon sanidine standard. Measurement control and data reduction were done using an in-house software suite that includes full error propagation by Monte Carlo procedures. Uncertainties are shown at the 95% confidence level.

Electron microprobe analyses of amphiboles, fluorapatites and monazites in representative thin sections were carried out using a CAMECA SX100, equipped with four WDS spectrometers which contain TAP, LIF, LLIF, PET, LPET, PC1, PC2 and PC3 crystals, housed at the central analytical facility of the University of Johannesburg. Analytical conditions are 15 kV accelerating voltage, 20 nA beam current, counting times of 10 to 20s for most elements, except 50s for F and 30s for Cl, and 1 to 5µm beam spot size were used. The following standards were used for calibration: fluorite for F (PC1 crystal); jadeite for Na, forsterite for Mg, almandine for Al and diopside for Si (TAP crystal); sodium chloride for Cl, orthoclase for K, wollastonite for Ca, metallic vanadium for V and barite for Ba (PET crystal); chromite for Cr, rhodonite for Mn, hematite for Fe, metallic cobalt for Co, nickel oxide for Ni and sphalerite for Zn (LLIF crystal). In addition for monazite analyses, a combination of well-characterized natural and synthetic standards including cheralite (Th), UO_2 (U), and synthetic (Y + REE) phosphates were used for calibration. Analytical errors for Y, the REE, Th, and other heavy elements depend on the absolute abundances of each element. Where possible, elongated fluorapatite grains, likely to be oriented parallel to c-axis, were chosen for analysis so as to minimize the increase in F X-ray excitation with time during microprobe analysis (e.g., Pyle et al., 2002).

For whole-rock geochemical analyses, the representative portion of the tonalitic vein (with both orthopyroxene-bearing and orthopyroxene-absent domains) was drilled out using a hand drill. Microdrill was employed to separate the composite domain representing melt-bearing portion adjacent to orthopyroxene with retrogressed margins. Major element contents for the sample was determined by X-ray fluorescent spectrometry at the ACT Labs, Canada, on glass beads prepared from powdered whole-rock sample with a sample-to-flux (lithium tetraborate) ratio of 1:10. Volatiles were determined by loss on ignition.